

Lateral Heterostructure Field-Effect Transistors Based on 2D-Material Stacks With Varying Thickness and Energy Filtering Source

E. G. Marin,^{†,‡} D. Marian,[†] M. Perucchini,[†] G. Fiori,[†] and G. Iannaccone^{*,†}

[†]*Dipartimento di Ingegneria dell'Informazione, Università di Pisa, 56122, Pisa, Italy*

[‡]*Dpto. Electrónica, Fac. Ciencias, Universidad de Granada, 18071, Granada, Spain*

E-mail: giuseppe.iannaccone@unipi.it

Abstract

The bandgap dependence on the number of atomic layers of some families of 2D-materials, can be exploited to engineer and use lateral heterostructures (LHs) as high-performance Field-Effect Transistors (FET). This option can provide very good lattice matching as well as high heterointerface quality. More importantly, this bandgap modulation with layer stacking can give rise to steep transitions in the density of states (DOS) of the 2D material, that can eventually be used to achieve sub-60 mV/decade subthreshold swing in LH-FETs thanks to an energy-filtering source. We have observed this effect in the case of a PdS₂ LH-FET due to the particular density of states of its bilayer configuration. Our results are based on *ab initio* and multiscale materials and device modeling, and incite the exploration of the 2D-material design space in order to find more abrupt DOS transitions and better suitable candidates.

Semiconductor heterostructures of the III-V and II-VI materials systems have played a fundamental role in the progress of electronics and optoelectronics. Firstly proposed by Kroemer in the 1950s,¹ they have been involved in the invention of quantum-well lasers² and high-electron-mobility transistors.³ The large number of available two-dimensional (2D) materials and the possibility to combine them even in the presence of significant lattice mismatch has led to a new wave of interest in materials engineering based on heterostructures of 2D materials. In particular, 2D materials enable the realization of vertical heterostructures, also called “van der Waals” heterostructures, consisting in the vertical stacking of layers of different 2D materials loosely coupled by van der Waals interactions,^{4,5} and of lateral heterostructures (LHs), in which a single 2D layer consists of juxtaposed regions of different lattice-matched 2D materials.^{6–9}

LHs have been shown to be particularly well suited as channel materials in high performance Field-Effect Transistors (FETs) for digital electronics.¹⁰ However, the quality of the heterojunction is one of the major obstacles towards the experimental demonstration of high performance LH-FETs. The possibility of fabricating LHs by modulating the stacking order of a single 2D material provides the opportunity of perfect lattice matching and growth compatibility, and therefore a chance to obtain high materials quality.¹¹

Recently, a particular group of transition metal dichalcogenides (TMDs) involving noble transition metals (Pt, Pd, and Ni), combined with S, Se, and Te, have been predicted¹² and demonstrated to have strong gap dependence on the number of stacked layers.¹³ The so-called “noble TMDs” are, thus, promising contenders to build 2D LHs by modulation of the number of layers of adjacent regions of the same material. Indeed, these structures based on noble TMDs –that strictly speaking could be considered homostructures instead of heterostructures– would be easier to realize than those made of different 2D materials. *Ab initio* calculations predict that the bandgap is reduced of more than 1 eV when these noble TMDs vary from monolayer (1L) to bilayer (2L), leading in some cases to a change of electronic phase from semiconductor to metal.^{12,14} Monolayer and few-layer PtS₂ and

PtSe₂ have already been synthesized,¹⁵⁻¹⁷ and devices such as Schottky barrier diodes on silicon have been fabricated.¹⁸ More recently, FETs made of few-layer PdSe₂ and PtSe₂ have been experimentally realized showing ambipolar transfer characteristics^{13,19,20} and a large dependence of PtSe₂ conductance on the number of layers has been observed.¹³

There is an additional advantage of some noble TMDs in their bilayer form: their density of states (DOS) exhibits a steep non-monotonic variation around the Fermi energy that can be used as an energy filtering mechanism in order to obtain a subthreshold swing (SS) of the FET smaller than the Boltzmann limit of 60 mV/decade at room temperature. Indeed, in thermionic FETs the inverse of the maximum slope of the current-voltage characteristics is limited to $SS = k_B T / q \ln(10)$ per decade, where k_B is Boltzmann constant, q is the elementary charge, and T is the absolute temperature.²¹⁻²³ This provides a room temperature SS value of $= 60$ mV/decade. A lower value can only be obtained if 1) injection is energy-constrained, such as in a Tunnel FET^{24,25} or using impact ionization,²⁶ or 2) if an effective negative capacitance is realized in the gate oxide stack, thus amplifying the surface potential at the channel.^{27,28} In particular, the energy-constrained injection from a steep DOS source has been demonstrated very recently using a graphene source in combination with a CNT channel in²¹ or a MoS₂ channel in.^{22,23} We show here that this effect can be achieved in a system based on a single 2D material, specifically PdS₂, where a bilayer source (injecting into a monolayer channel) can provide sufficient energy filtering to yield an SS below the Boltzmann limit.

In this work we investigate the potential of noble TMDs as channel materials for LH-FETs, showing the possibility to engineer an energy-filtering source in order to obtain sub-60 mV/dec SS at room temperature and to design devices with competitive figures of merit when compared to the predictions of the International Roadmap for Devices and Systems (IRDS).²⁹ Finally, we show that noble TMDs enable the realization of a 2D resonant tunneling diode (RTD) based on LHs obtained with modulation of the number of atomic layers.

Results and discussion

Lateral Heterostructure FETs

We have selected those noble TMDs exhibiting a sharp non-monotonic DOS around the Fermi level and therefore potentially able to achieve $SS < 60$ mV/decade at room temperature. Following bandstructure calculations available in the literature,^{11,14} we have opted for PdS₂ and NiS₂. Both materials are semimetal in bilayer form and semiconductors in monolayer form, so it is possible to build a FET with a lateral heterostructure formed by a bilayer source, a monolayer central channel region, and a bilayer drain. This results in two semimetal-semiconductor Schottky barriers at the source and drain ends. For the sake of clarity, a semimetal is a material with zero gap but a relatively low density of states around the Fermi energy. We have also considered PtS₂ which presents a strong modulation of the bandgap from monolayer to bilayer, still maintaining a semiconducting gap.

We have adopted a multi-scale simulation approach combining different levels of physical abstraction, ranging from *ab initio* calculations of materials properties to full device simulations based on coherent quantum transport.³⁰ We have calculated the electronic bandstructure of monolayer and bilayer PdS₂, PtS₂, and NiS₂ using density functional theory (DFT) as implemented in the Quantum Espresso suite³¹ (see Methods). The strong dependence of the electronic structure on the number of layers is highlighted in Fig. 1(a): when the crystal structure is varied from monolayer to bilayer, PdS₂ and NiS₂ undergo a phase change from semiconductor to semimetal, whereas PtS₂ has its energy gap reduced from 1.59 eV to 0.48 eV. The drastic variation of the DOS of bilayer PdS₂ and NiS₂ around the Fermi level can be exploited to inject carriers from the source with sub-maxwellian energy tails, leading to $SS < 60$ mV/decade at room temperature.

The plane-wave DFT basis set has been translated into a Maximally-Localized-Wannier-Functions (MLWFs) basis set by means of the Wannier90 code,³² that provides us with tight-binding (TB) Hamiltonians for every material and stacking (see Methods and Fig. S1

in the Supplementary Information). The TB Hamiltonians are then employed to build a total Hamiltonian of the lateral heterostructure devices, following the procedure developed and validated in³³ (Fig. 1(b) and Methods). In order to accurately model the Schottky barrier formed at the bilayer/monolayer interfaces we have performed an energy analysis from first-principles taking into account the band offsets and the formation of dipoles³⁴ (see Supplementary Information).

The considered LH-FETs are also illustrated in Fig. 1(c). The length of the bilayer source and drain regions are $L_{s/d} = 11$ nm, 10.4 nm and 16.7 nm for PdS₂, NiS₂, and PtS₂ respectively. They are assumed to be ohmically contacted by the external metal leads with work-functions 5.6 eV and 5.8 eV for PdS₂ and NiS₂, respectively, and 5.3 eV/6.0 eV for the *n*-type/*p*-type PtS₂. The monolayer 2D channel, with length L_{ch} , is embedded in top and bottom SiO₂, with thickness $t_{ox} = 0.5$ nm.

Sketches of the band-edge profiles of the PdS₂ and NiS₂ LH-FETs with semimetal source and drain are shown in Fig. 1(d); the PtS₂ LH-FET with small gap source and drain is shown in Fig. 1(e). The complete MLWF Hamiltonian describing the channel including source and drain regions feeds the open-boundary Schrödinger equation, within the Non-equilibrium Green Functions (NEGF)³⁵ formalism, that is self-consistently solved with the electrostatics of the whole device (see Methods).^{36,37}

In order to study the potential performance of the considered LH-FETs for logic applications, we set a supply voltage $V_{dd} = 0.5$ V, and we simulate the transfer characteristics for a drain-to-source voltage $V_{DS} = V_{dd}$. Those are shown in Fig. 6 in semilogarithmic scale for channel lengths ranging from $L_{ch} \simeq 5$ nm up to $L_{ch} \simeq 10$ nm and for the three different materials. As it can be seen, the bilayer metallic source/drain regions in PdS₂ and NiS₂ lead to an ambipolar behavior. For channel lengths longer than 10 nm, I_{off} is not further reduced, being the ambipolarity determined by the bandgap of the monolayer channel and the capability of the bilayer source to inject both kinds of carriers. In this regard, some improvement might be achieved following the back-gate over/underlapping strategy at the

source/drain discussed in Ref.³⁸ Here we have tuned the gate workfunction in the PdS₂ and NiS₂ devices to 5.52 eV so to observe the crossover between *n*-type and *p*-type conduction at $V_{\text{GS}} = 0$ V.

The PtS₂ LH-FET is not ambipolar since it has semiconductor source and drain. In this case we show in Fig. 6(c) and (d) both the nFET and the pFET characteristics, where the gate workfunction is tuned to 5.28 eV and 6.2 eV, respectively, to obtain the current in the OFF state $I_{\text{off}} = 100$ nA/ μm at $V_{\text{GS}} = 0$ V, as required by the IRDS²⁹ for high performance applications where the OFF state corresponds to $V_{\text{GS}} = 0$ V and $V_{\text{DS}} = \pm V_{\text{dd}}$. The source and drain regions have a donor doping with molar fraction $N_{\text{D}} = 4.1 \times 10^{-2}$ in the case of nFET, and acceptor molar fraction $N_{\text{A}} = 9.5 \times 10^{-2}$ in the case of pFET. The channel is undoped for all devices.

Interestingly, the *p*-type branch of the PdS₂ LH-FET $I_{\text{DS}} - V_{\text{GS}}$ curve exhibits a sub-maxwellian SS down to 52 mV/decade, as shown in Fig. 3(a). The possibility to achieve sub-60 mV/decade SS in a thermionic FET has been subject of debate.^{39,40} In particular, in Ref.⁴⁰ the authors argue that the 60 mV/decade limit cannot be beaten in a single barrier device, although they eventually conclude that the role of the DOS can be essential to reverse this situation, as has already been experimentally demonstrated in the case of a graphene source.²¹

We can discuss the specific mechanism in the PdS₂ LH-FET by considering the band edge profiles shown in Fig. 4(a) for $V_{\text{DS}} = V_{\text{dd}}$ and for three different values of V_{GS} in the subthreshold region of the *p*-type branch. The Schottky barriers of drain-channel and source-channel junctions are calculated from first-principles (see Supplementary Information). A variation of V_{GS} modulates both the conduction and valence band edges in the channel and the transparency of the Schottky barrier between source and channel. The drop of the DOS in the source for energy below the source Fermi level (corresponding to -0.5 eV for the considered bias point) is clearly visible in Fig. 4(b), (where the DOS is obtained from refined calculations applying, for visualization purposes, a Gaussian smoothing with $\sigma = 10$ meV

–see Supporting Information–) and is responsible for a sharper energy filtering than that provided by the Maxwell-Boltzmann tail of the occupation factor, and therefore for an SS lower than the so-called Boltzmann limit. This is even more apparent by considering the energy spectrum of the current —*i.e.* the current density per unit energy— for different values of V_{GS} shown in Fig. 4(c). The slope of the logarithm of the current spectrum as a function of energy would be exactly $-1/(k_B T)$ for a constant DOS, corresponding to one decade every 60 meV at room temperature. Due to the non-constant DOS in the source, such slope is however not constant, and in one decade around an energy of -0.7 eV, where the DOS is dramatically quenched, it is in the range of 30 meV to 50 meV, marked as a shaded region in Fig. 4(c). This more confined current spectrum is responsible for the sub-Maxwellian subthreshold swing of the p -type branch transfer characteristics of the PdS₂ LH-FET.

Energy filtering is not observed in the n -branch because the DOS of the conduction band states in PdS₂ do not show a similar steep transition (see the Supporting Information for more details). The effect is neither observed in NiS₂ where the small gap of the monolayer semiconductor results in large interband tunneling currents and very poor SS (above 200 meV/decade and therefore not shown in Fig. 3(a)). The PtS₂ LH-FET has a close to ideal Maxwellian SS of 60 mV/decade for HP applications due to the dominant Fermi window tail that restricts the SS.

Other transistor figures of merit for digital electronics are considered in Fig. 3 following the IRDS specifications for high-performance (HP) applications. In particular, Fig. 3(b) shows I_{on}/I_{off} ratio, where I_{on} is the drain current in the ON state – corresponding to $V_{GS} = V_{DS} = \pm V_{dd}$ and $I_{off} = 100$ nA/ μm is the current in the OFF state as defined by the IRDS for HP. To this purpose, the PdS₂ LH-FET exhibits the highest I_{on}/I_{off} ratio for channel length close to 10 nm thanks to the lower SS just discussed, but not for shorter channel lengths (down to 5 nm), because of the high I_{off} due to ambipolarity and large source-to-drain tunneling. The situation is worse for the NiS₂ LH-FET: its smaller monolayer

bandgap (0.47 eV) leads to a very poor $I_{\text{on}}/I_{\text{off}}$ ratio. The PtS₂ LH-FET, instead, has a semiconducting bandgap and negligible source-to-drain tunneling, and therefore exhibits high $I_{\text{on}}/I_{\text{off}}$ ratio for L_{ch} down to 5 nm.

Relevant figures of merit for transistor performance in digital circuits are also the intrinsic delay time $\tau = (Q_{\text{on}} - Q_{\text{off}})/I_{\text{on}}$ and the Power-Delay-Product $\text{PDP} = V_{\text{dd}}\tau I_{\text{on}}$, where Q_{on} and Q_{off} are the total mobile charge in the channel in the ON and OFF states, respectively (Fig. 3(c) and 3(d)). The nFETs based on PdS₂ and PtS₂ exhibit expected τ and PDP compliant with IRDS requirements for next technology nodes,^{10,29} together with an $I_{\text{on}}/I_{\text{off}}$ ratio close to 10^4 for channel lengths of at least 10 nm, which implies acceptable stand-by power consumption for HP applications.²⁹ The pFETs have slightly worse PDP and τ than the nFETs, due to the smaller source DOS in the valence band – apparent in Fig. 1(a) – which is responsible for a smaller I_{on} , as can be seen in the asymmetric transfer characteristics of Fig. 6.

While the ambipolarity of PdS₂ and NiS₂ FETs spoils their use in low power (LP) applications, PtS₂ FETs also satisfy the IRDS requirements to this purpose (*i.e.* they reach an $I_{\text{off}} = 100$ pA/ μm) achieving $I_{\text{on}}/I_{\text{off}}$ ratios above 10^6 and 10^5 for *n*-type and *p*-type FETs, respectively (see Supporting Information). For low stand-by power, SS is spoiled in shorter channel lengths since the tunneling current becomes comparable to the pursued I_{off} : for $L_{\text{ch}} \approx 5 - 8$ nm it is in the range 80-100 mV/decade for nFETs and 70-90 mV/decade for pFETs, deviating considerably from the 60 mV/decade observed in longer channels. Finally, the PDP is slightly lower and the intrinsic delay time slightly higher than the values obtained for HP (see Supporting Information for details).

Resonant Tunneling Diode

Finally, we have studied the operation of a 2D Resonant Tunneling Diode based on a PtS₂ LH (LH-RTD). We have considered bilayer PtS₂ drain and source regions with length 11.2 nm. Two monolayer regions act as energy barriers confining a bilayer well. The barrier length

is $L_b = 1.9$ nm and the length of the well L_w is varied from 1.9 nm up to 5.6 nm. The whole 2D channel is embedded in SiO_2 . Fig. 9(a) shows the I_{DS} vs V_{DS} characteristics for $L_w = 1.9$ nm at room temperature. The current has a clear non-monotonic behavior exhibiting a pronounced negative differential resistance, due to resonant tunneling through quantized states in the 2D well. The local DOS in the channel is plotted in Fig. 9(b) as a function of energy and of position along the device length (y) for $V_{\text{DS}} = 0.25$ V and 0.5 V, corresponding to the main peak and to the valley of the current-voltage characteristics. Let us stress the fact that the bandstructure of different regions is fully considered in the calculation, but inelastic processes and heterojunction defects are not included.

The Fermi level at the source (μ_s) and drain (μ_d) leads are marked. We have superimposed the conduction and valence band profiles to the local DOS colormaps. The alignment of μ_s with these quantized energy levels results in resonances in the current spectrum density and is controlled by V_{DS} . We have also explored different well lengths: $L_w = 1.9$ nm, 3.7 nm and 5.6 nm (Fig. 9(c)), observing that the NDR effect is preserved, although the position of the peak varies with the well length as so does the energy quantization, while the position of the valley is not modified as it depends on the height of the barrier limiting the thermionic emission.

Conclusion

We have shown that the strong dependence of the bandgap upon the number of layers of noble TMDs can be used to devise electron devices based on transport through lateral heterostructures of TMDs, such as LH-FETs and LH-RTDs.

We have used *ab-initio* multiscale simulations to demonstrate that LH-FETs based on PdS_2 and PtS_2 can comply with IRDS performance requirements²⁹ for future integrated circuit technology for high performance digital applications. On the other hand, LH-FETs made of NiS_2 cannot meet such requirements, due to the low gap and ambipolar behavior.

We have also predicted the steep (submaxwellian) subthreshold behavior of p -type FETs based on PdS₂, due to the asymmetry of the bilayer PdS₂ DOS around the Fermi level, achieving SS=52 mV/decade. This is the first demonstration of this effect in an intrinsic 2D material, and can be further exploited for device design. It must be noted that in presence of electron-electron or electron-phonon scattering the behavior of the studied devices would be degraded with respect to the optimum ballistic condition assumed here, impacting directly on the achieved sub-Boltzmann slope. Moreover, the SS value for PdS₂ FETs is not expected to boost the device performance stunningly as compared to the conventional limit. However, and more importantly, the results presented here confirm that the 60mV/decade limit can be beaten in 2D-based FETs, as it has been proved experimentally in graphene, encouraging the exploration of new 2D materials with sharper DOS and consequently steeper SSs.

Finally, we have also predicted the possibility of using 2D LHs to obtain a resonant tunneling diode, with a pronounced peak-to-valley ratio of the current-voltage characteristics, which is suitable for experimental observation.

Methods

Density Functional Theory as implemented in Quantum Espresso code has been employed to determine the electronic structure of PdS₂, NiS₂ and PtS₂. The crystal geometry of monolayer and bilayer 2D crystals is characterized by a 1T arrangement, with a layer of Pt/Pd/Ni atoms sandwiched between two atomic layers of S atoms. The atoms coordinates and lattice vectors has been obtained after,¹⁴ where a structural optimization of the unitary cell was performed. We have considered 40 Å of vacuum in the direction orthogonal to the 2D layers to minimize spurious interactions between periodic repetitions of the cell. For the exchange-correlation functional, the local density approximation has been considered under the Perdew-Zunger⁴¹ parametrization within norm-conserving pseudopotentials. The energy cutoffs for charge density and wavefunction expansions have been set to 360 Ry and 60 Ry

respectively. A Monkhorst–Pack $10 \times 5 \times 1$ k -mesh has been used for the Brillouin-zone integration and an energy convergence threshold of 10^{-6} eV in the iterative solution of the Kohn-Sham equations was ensured. Additionally, an analysis of the Schottky barriers formed at the 2L/1L heterojunction has been performed (see Supplementary Information).

Maximally-Localized-Wannier-Functions (MLWFs) have been obtained by means of the Wannier90 code³² for every material and stacking. For the change of basis, the same k -sampling of the Brillouin zone as in the DFT simulations has been used to compute the overlap matrices required to determine the MLWFs. 12 bands around the fundamental gap have been considered and a threshold of 10^{-10} Å has been set for the total spread change in the MLWFs in 20 consecutive iterations. The MLWFs band-structures have been calculated along the same path as in DFT, showing very good agreement (see Supplementary Information Fig. S1). The MLWF Hamiltonians of the 1L and 2L regions have been employed to build the total Hamiltonian of the lateral heterostructure following the procedure presented in Ref.³³

The device simulations consist of the self-consistent solution of the open-boundary Schrödinger equation, within the Non-equilibrium Green Functions (NEGF)³⁵ formalism, and the Poisson equation, for which we have used the open-source code NanoTCAD ViDES.^{36,37} The construction of the Hamiltonian of the heterostructure from the Hamiltonians of the different regions/materials requires a careful treatment, with special attention to the mixing of the interface elements. We have followed the procedure we developed and validated in Ref.³³ In particular, the off-diagonal elements connecting the 1L and 2L regions and determining their coupling have been assumed to be equal to those of the monolayer region. We have tested different alternatives for the off-diagonal coupling elements at the interface (see Supplementary Information) observing little variation in the device behavior. This mixing procedure provides the best results in terms of robustness in the convergence, preserving computational accuracy as compared to *ab-initio* simulations. For all devices we have considered operation at temperature of 300 K.

Acknowledgement

Authors gratefully acknowledge the support from the European Commission through the Graphene Flagship Core 2 (contract n. 785219) and through the QUEFORMAL h2020 Project (contract n. 829035). E.G. Marin also acknowledges Juan de la Cierva Incorporación IJCI-2017-32297 (MINECO/AEI)

References

1. Kroemer, H. Nobel Lecture: Quasielectric Fields and Band Offsets: Teaching Electrons New Tricks. *Rev. Mod. Phys.* **2001**, *73*, 783–793.
2. van der Ziel, J. P.; Dingle, R.; Miller, R. C.; Wiegmann, W.; Nordland, W. A. Laser Oscillation From Quantum States in Very Thin GaAs-Al_{0.2}Ga_{0.8}As Multilayer Structures. *Appl. Phys. Lett.* **1975**, *26*, 463–465.
3. Mimura, T.; Hiyamizu, S.; Fujii, T.; Nanbu, K. A New Field-Effect Transistor With Selectively Doped GaAs/*n*-Al_{*x*}Ga_{1-*x*}As Heterojunctions. *Jpn. J. Appl. Phys.* **1980**, *19*, L225–L227.
4. Geim, A. K.; Grigorieva, I. V. Van Der Waals Heterostructures. *Nature* **2013**, *499*, 419.
5. Novoselov, K. S.; Mishchenko, A.; Carvalho, A.; Castro Neto, A. H. 2D Materials and Van Der Waals Heterostructures. *Science* **2016**, *353*, aac9439.
6. Ci, L.; Song, L.; Jin, C.; Jariwala, D.; Wu, D.; Li, Y.; Srivastava, A.; Wang, Z. F.; Storr, K.; Balicas, L. *et al.* Atomic Layers of Hybridized Boron Nitride and Graphene Domains. *Nat. Mater.* **2010**, *9*, 430.
7. Levendorf, M. P.; Kim, C.-J.; Brown, L.; Huang, P. Y.; Havener, R. W.; Muller, D. A.; Park, J. Graphene and Boron Nitride Lateral Heterostructures for Atomically Thin Circuitry. *Nature* **2012**, *488*, 627.

8. Liu, Z.; Ma, L.; Shi, G.; Zhou, W.; Gong, Y.; Lei, S.; Yang, X.; Zhang, J.; Yu, J.; Hackenberg, K. P. *et al.* In-Plane Heterostructures of Graphene and Hexagonal Boron Nitride With Controlled Domain Sizes. *Nat. Nanotechnol.* **2013**, *8*, 119.
9. Huang, C.; Wu, S.; Sanchez, A. M.; Peters, J. J.; Beanland, R.; Ross, J. S.; Rivera, P.; Yao, W.; Cobden, D. H.; Xu, X. Lateral Heterojunctions Within Monolayer MoSe₂–WSe₂ Semiconductors. *Nat. Mater.* **2014**, *13*, 1096.
10. Iannaccone, G.; Bonaccorso, F.; Colombo, L.; Fiori, G. Quantum Engineering of Transistors Based on 2D Materials Heterostructures. *Nat. Nanotechnol.* **2018**, *13*, 183–191.
11. Ghorbani-Asl, M.; Kuc, A.; Mir, P.; Heine, T. A Single-Material Logical Junction Based on 2D Crystal PdS₂. *Adv. Mater.* **2016**, *28*, 853–856.
12. Wang, Y.; Li, Y.; Chen, Z. Not Your Familiar Two Dimensional Transition Metal Disulfide: Structural and Electronic Properties of the PdS₂ Monolayer. *J. Mater. Chem. C* **2015**, *3*, 9603–9608.
13. Ciarrocchi, A.; Avsar, A.; Ovchinnikov, D.; Kis, A. Thickness-Modulated Metal-To-Semiconductor Transformation in a Transition Metal Dichalcogenide. *Nat. Commun.* **2018**, *9*, 919.
14. Mir, P.; Ghorbani-Asl, M.; Heine, T. Two Dimensional Materials Beyond MoS₂: Noble-Transition-Metal Dichalcogenides. *Angew. Chem., Int. Ed. Engl.* **2014**, *53*, 3015–3018.
15. Zhao, Y.; Qiao, J.; Yu, P.; Hu, Z.; Lin, Z.; Lau, S. P.; Liu, Z.; Ji, W.; Chai, Y. Extraordinarily Strong Interlayer Interaction in 2D Layered PtS₂. *Adv. Mater.* **2016**, *28*, 2399–2407.
16. Wang, Y.; Li, L.; Yao, W.; Song, S.; Sun, J. T.; Pan, J.; Ren, X.; Li, C.; Okunishi, E.; Wang, Y.-Q. *et al.* Monolayer PtSe₂, a New Semiconducting Transition-Metal-

- Dichalcogenide, Epitaxially Grown by Direct Selenization of Pt. *Nano Lett.* **2015**, *15*, 4013–4018.
17. Yan, M.; Wang, E.; Zhou, X.; Zhang, G.; Zhang, H.; Zhang, K.; Yao, W.; Lu, N.; Yang, S.; Wu, S. *et al.* High Quality Atomically Thin PtSe₂ Films Grown by Molecular Beam Epitaxy. *2D Mater.* **2017**, *4*, 045015.
 18. Yim, C.; Lee, K.; McEvoy, N.; O'Brien, M.; Riazimehr, S.; Berner, N. C.; Cullen, C. P.; Kotakoski, J.; Meyer, J. C.; Lemme, M. C. *et al.* High-Performance Hybrid Electronic Devices From Layered PtSe₂ Films Grown at Low Temperature. *ACS Nano* **2016**, *10*, 9550–9558.
 19. Chow, W. L.; Yu, P.; Liu, F.; Hong, J.; Wang, X.; Zeng, Q.; Hsu, C.-H.; Zhu, C.; Zhou, J.; Wang, X. *et al.* High Mobility 2D Palladium Diselenide Field-Effect Transistors With Tunable Ambipolar Characteristics. *Adv. Mater.* **2017**, *29*, 1602969.
 20. Zhao, Y.; Qiao, J.; Yu, Z.; Yu, P.; Xu, K.; Lau, S. P.; Zhou, W.; Liu, Z.; Wang, X.; Ji, W. *et al.* High-Electron-Mobility and Air-Stable 2D Layered PtSe₂ FETs. *Adv. Mater.* **2017**, *29*, 1604230.
 21. Qiu, C.; Liu, F.; Xu, L.; Deng, B.; Xiao, M.; Si, J.; Lin, L.; Zhang, Z.; Wang, J.; Guo, H. *et al.* Dirac-Source Field-Effect Transistors as Energy-Efficient, High-Performance Electronic Switches. *Science* **2018**, *361*, 387–392.
 22. Liu, F.; Qiu, C.; Zhang, Z.; Peng, L.; Wang, J.; Guo, H. Dirac Electrons at the Source: Breaking the 60-mV/Decade Switching Limit. *IEEE Trans. Electron Devices* **2018**, *65*, 2736–2743.
 23. Logoteta, D.; Pala, M. G.; Choukroun, J.; Dollfus, P.; Iannaccone, G. A Steep-Slope MoS₂-Nanoribbon MOSFET Based on an Intrinsic Cold-Contact Effect. *IEEE Electron Device Lett.* **2019**, *40*, 1550–1553.

24. Appenzeller, J.; Lin, Y.-M.; Knoch, J.; Avouris, P. Band-To-Band Tunneling in Carbon Nanotube Field-Effect Transistors. *Phys. Rev. Lett.* **2004**, *93*, 196805.
25. Seabaugh, A. C.; Zhang, Q. Low-Voltage Tunnel Transistors for Beyond CMOS Logic. *Proc. IEEE* **2010**, *98*, 2095–2110.
26. Gopalakrishnan, K.; Griffin, P. B.; Plummer, J. D. I-Mos: A Novel Semiconductor Device With a Subthreshold Slope Lower Than kT/q . Digest. International Electron Devices Meeting,. 2002; pp 289–292.
27. Salahuddin, S.; Datta, S. Use of Negative Capacitance to Provide Voltage Amplification for Low Power Nanoscale Devices. *Nano Lett.* **2008**, *8*, 405–410.
28. Salvatore, G. A.; Bouvet, D.; Ionescu, A. M. Demonstration of Subthreshold Swing Smaller Than 60mV/Decade in Fe-Fet With P (VDF-TrFE)/SiO₂ Gate Stack. 2008 IEEE Int. Electron Devices Meet. 2008; pp 1–4.
29. International Roadmap for Devices and Systems, 2018 Edition Available At:. <https://irds.ieee.org/editions/2018>, Accessed: 2019-05-20.
30. Marin, E. G.; Perucchini, M.; Marian, D.; Iannaccone, G.; Fiori, G. Modeling of Electron Devices Based on 2-D Materials. *IEEE Trans. Electron Devices* **2018**, *65*, 4167–4179.
31. Giannozzi, P.; Baroni, S.; Bonini, N.; Calandra, M.; Car, R.; Cavazzoni, C.; Ceresoli, D.; Chiarotti, G. L.; Cococcioni, M.; Dabo, I. *et al.* QUANTUM ESPRESSO: A Modular and Open-Source Software Project for Quantum Simulations of Materials. *J. Phys.: Condens. Matter* **2009**, *21*, 395502.
32. Marzari, N.; Mostofi, A. A.; Yates, J. R.; Souza, I.; Vanderbilt, D. Maximally Localized Wannier Functions: Theory and Applications. *Rev. Mod. Phys.* **2012**, *84*, 1419–1475.
33. Marian, D.; Dib, E.; Cusati, T.; Marin, E. G.; Fortunelli, A.; Iannaccone, G.; Fiori, G.

- Transistor Concepts Based on Lateral Heterostructures of Metallic and Semiconducting Phases of MoS₂. *Phys. Rev. Applied* **2017**, *8*, 054047.
34. Katagiri, Y.; Nakamura, T.; Ishii, A.; Ohata, C.; Hasegawa, M.; Katsumoto, S.; Cusati, T.; Fortunelli, A.; Iannaccone, G.; Fiori, G. *et al.* Gate-Tunable Atomically Thin Lateral MoS₂ Schottky Junction Patterned by Electron Beam. *Nano Lett.* **2016**, *16*, 3788–3794.
35. Datta, S. Nanoscale Device Modeling: the Greens Function Method. *Superlattices Microstruct.* **2000**, *28*, 253 – 278.
36. Bruzzone, S.; Iannaccone, G.; Marzari, N.; Fiori, G. An Open-Source Multiscale Framework for the Simulation of Nanoscale Devices. *IEEE Trans. Electron Devices* **2014**, *61*, 48–53.
37. NanoTCAD ViDES Available At: <http://vides.nanotcad.com/vides/>, Accessed: 2019-05-20.
38. Wu, P.; Appenzeller, J. High Performance Complementary Black Phosphorus FETs and Inverter Circuits Operating at Record-Low v_{DD} Down to 0.2 V. 2018 76th Device Research Conference (DRC). 2018; pp 1–2.
39. Cheung, K. P. On the 60 mV/dec @300 K Limit for MOSFET Subthreshold Swing. *Proceedings of 2010 International Symposium on VLSI Technology, System and Application* **2010**, 72–73.
40. Solomon, P. M. Inability of Single Carrier Tunneling Barriers to Give Subthermal Subthreshold Swings in MOSFETs. *IEEE Electron Device Lett.* **2010**, *31*, 618–620.
41. Perdew, J. P.; Zunger, A. Self-Interaction Correction to Density-Functional Approximations for Many-Electron Systems. *Phys. Rev. B* **1981**, *23*, 5048–5079.

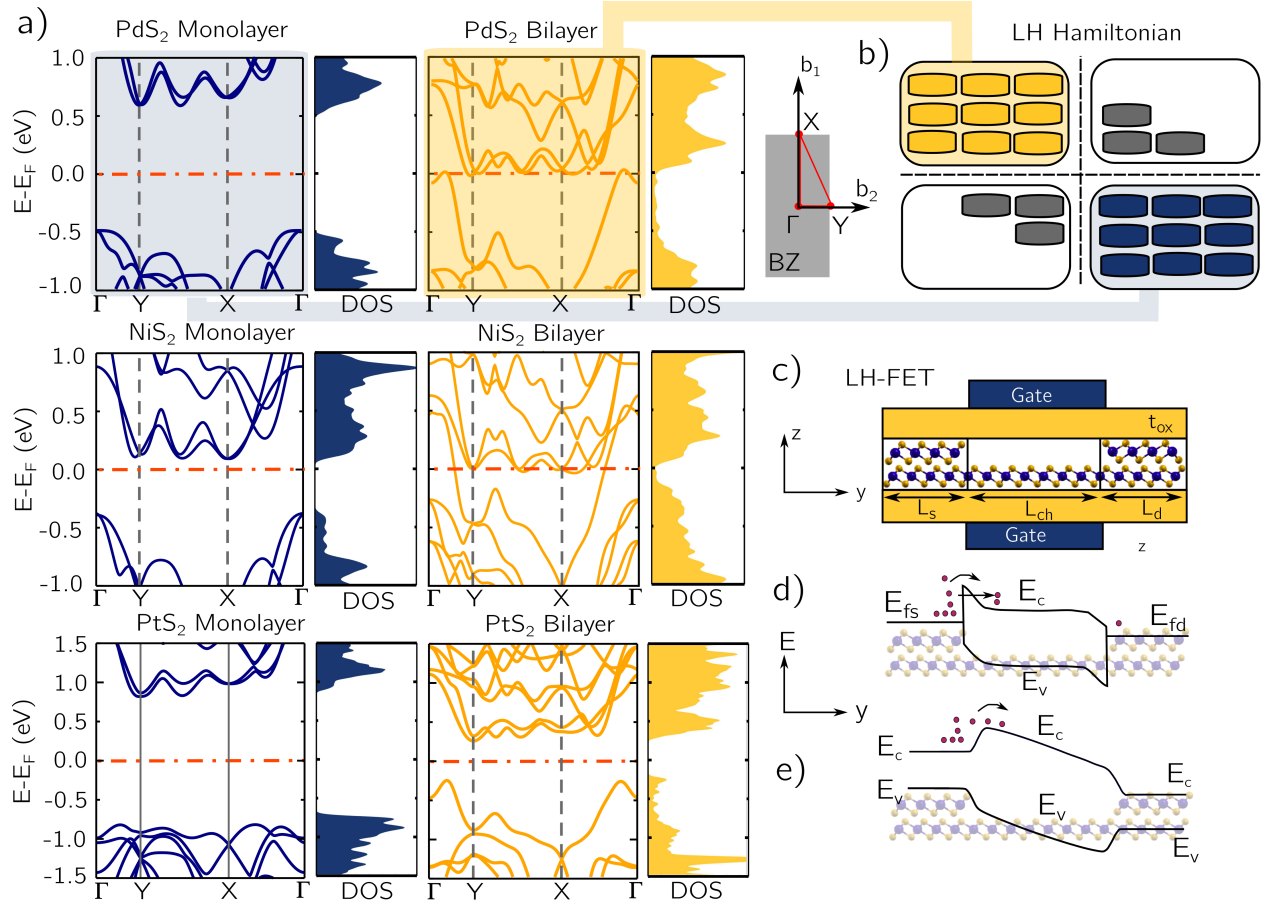


Figure 1: (a): Electronic band-structure on a highly symmetric path along the Brillouin zone depicted aside in gray with the path marked in red, and density of states integrated in the whole Brillouin zone, as computed with Density Functional Theory, for monolayer (1L) and bilayer (2L) PdS₂, NiS₂, and PtS₂. (b): Schematic representation of the construction of the lateral heterostructure Hamiltonian from the Hamiltonian of the bilayer and monolayer materials. (c): Schematic of the Lateral Heterostructure FET, with bilayer source, monolayer channel, and bilayer-drain. (d) Illustration of the energy band edge profile of the PdS₂ and NiS₂ LH-FETs, and (e) band edge profile of PtS₂ LH-FET.

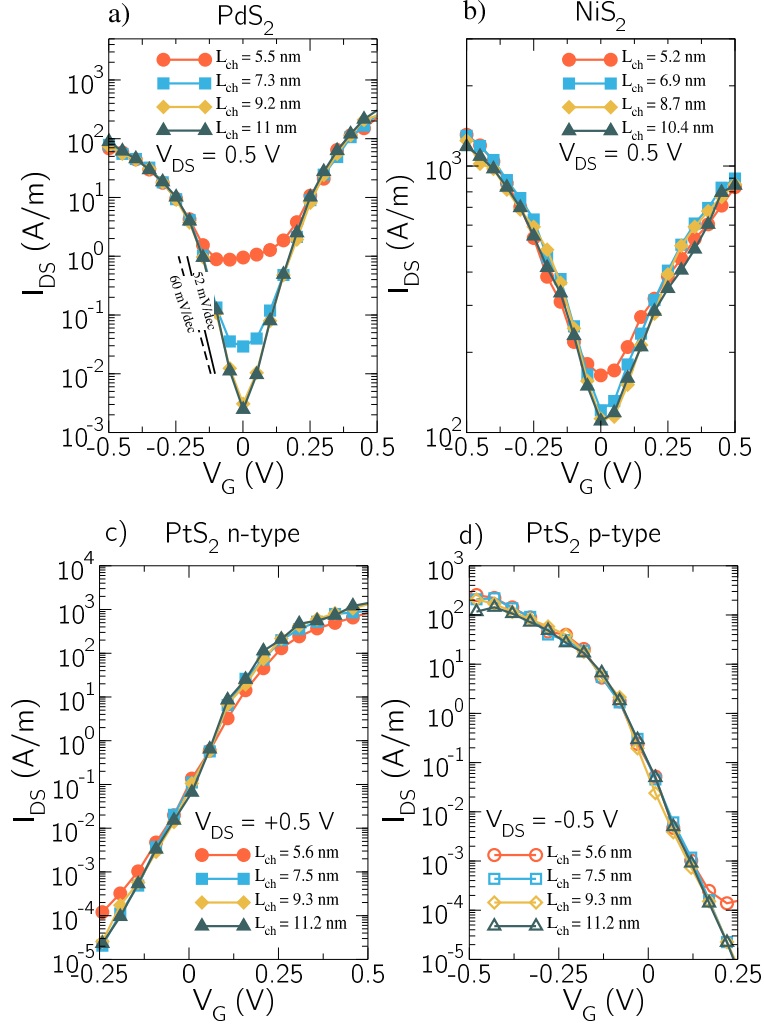


Figure 2: Transfer characteristic in semilogarithmic scale for the LH-FETs with PdS₂ (a), NiS₂ (b) and *p*-type/*n*-type PtS₂ (c)/(d) considering a channel length ranging from $\simeq 5$ nm up to $\simeq 10$ nm and drain-to-source voltage $|V_{DS}| = 0.5$ V. In the case of PdS₂ and NiS₂ an ambipolar behavior is observed due to the semimetallic source and drain. In the case of PtS₂ we consider both the nFET and the pFET. The channel is always undoped. A metal gate workfunction of 5.52 eV is assumed in the PdS₂ and NiS₂ devices to so to observe the crossover between *n*-type and *p*-type conduction at $V_{GS} = 0$ V. For the PtS₂ nFET and pFET, the gate workfunction is tuned to 5.28 eV and 6.2 eV, respectively, to set $I_{off} = 100$ nA/ μ m at $V_{GS} = 0$ V.

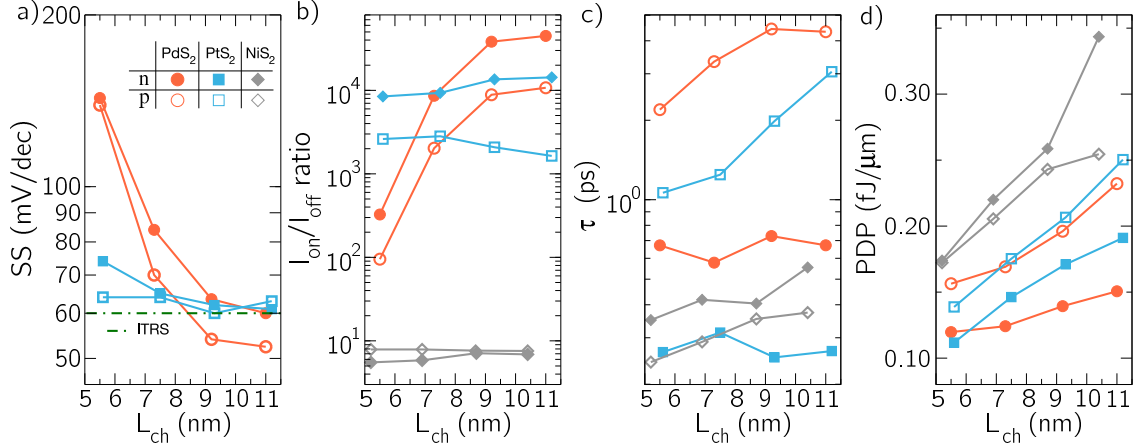


Figure 3: SS, $I_{\text{on}}/I_{\text{off}}$, τ and PDP as a function of the channel length, L_{ch} , for the LH-FETs based on PdS₂, PtS₂, and NiS₂, evaluated according to the IRDS requirements for high-performance applications: $I_{\text{off}} = 100\text{nA}/\mu\text{m}$.

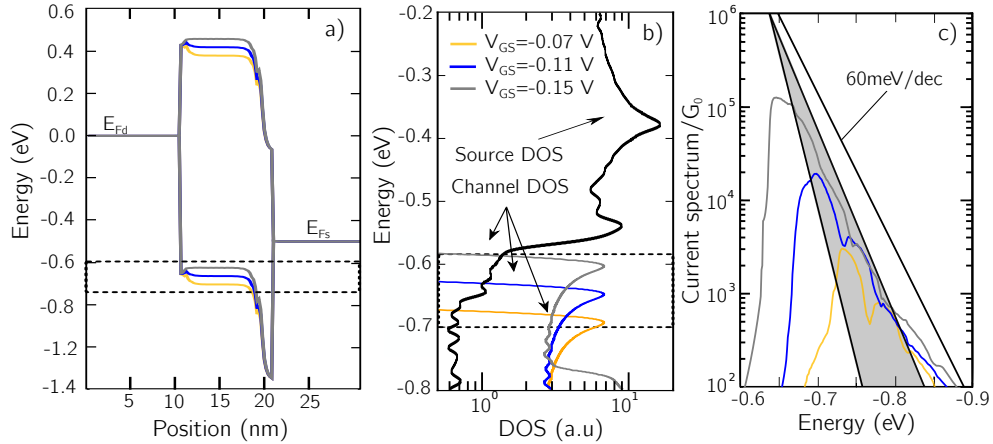


Figure 4: a): Conduction and valence band edge profiles of the PdS₂ LH-FET for $V_{\text{DS}} = -V_{\text{dd}}$ and three different values of $V_{\text{GS}} = -0.07, -0.11, -0.15$ V in the subthreshold region of the p-branch. b) Density of states of the source and of the channel for the corresponding values of V_{GS} obtained in a dense k-mesh grid, see Supporting Information, and after a Gaussian smoothing for the energy integration with $\sigma = 10$ meV; c) Current spectrum as a function of energy. In shaded gray the range of slopes between 30 mV/decade and 50 mV/decade. The 60 mV/decade Boltzmann limit is also plotted.

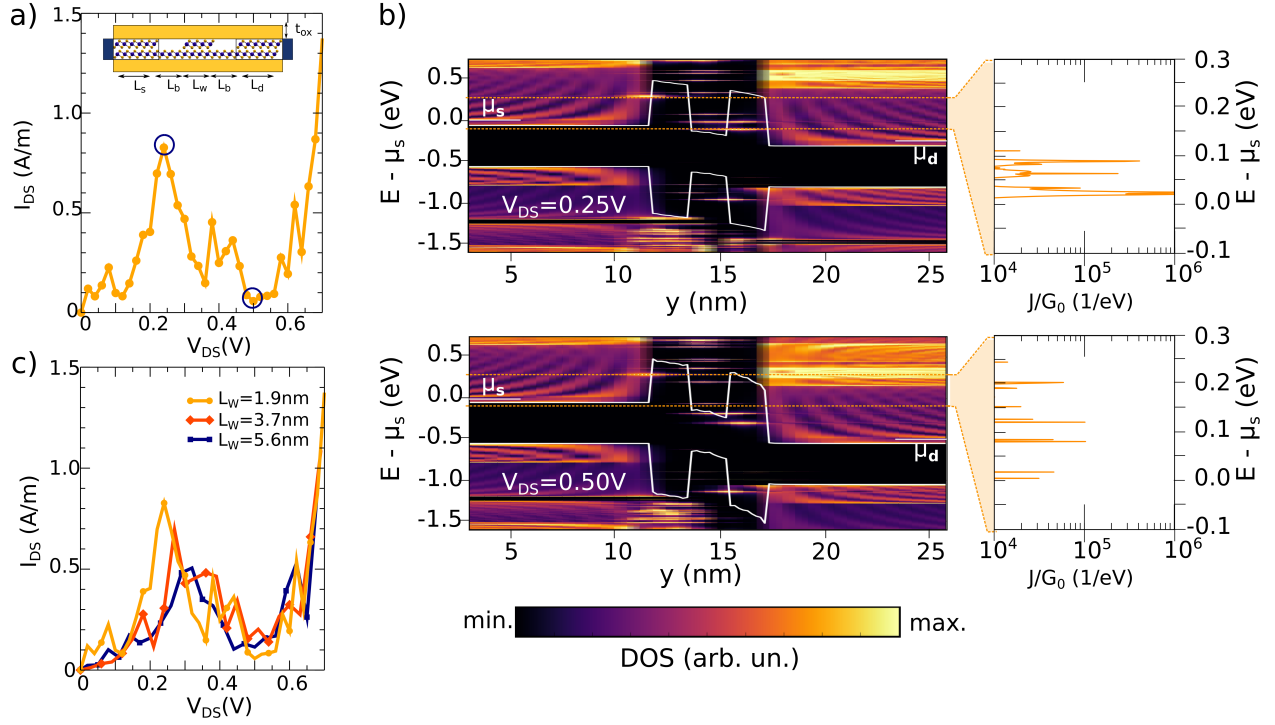


Figure 5: a) I_{DS} vs V_{DS} characteristic of the LH-RTD based on PtS_2 with $L_w = 1.9$ nm. Inset: Schematic of the Lateral Heterostructure RTD b) Local DOS as a function of the energy and the position along the device length, and current-density spectrum, normalized to the conductance quantum ($G_0 = 2q^2/\hbar$), for the RTD with a $L_w = 1.9$ nm, for $V_{DS} = 0.25$ V and 0.5 V. c) Current-voltage characteristics of the LH-RTD for different well lengths.

Supplementary Information

Hamiltonian of the lateral heterostructure

In order to build the heterostructure Hamiltonian, one must take notice of the off-diagonal elements connecting the monolayer and the bilayer regions. In particular, in the Hamiltonian along the transport direction each block represents a ($\#$ wannier centers \times $\#$ wannier centers) matrix, and the number of blocks along a row is constrained by the Monkhorst-Pack grid. The blocks in the off-diagonal elements connect a row of the bilayer region to a column of the monolayer region, i.e. they connect the last cell of the source and the first of the channel (and equivalently at the drain end).

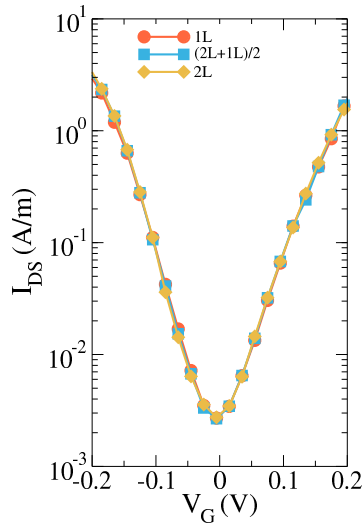


Figure 6: Transfer characteristic for the bilayer-monolayer-bilayer PdS₂ lateral-heterostructure FET with a channel length 9.2 nm assuming different coupling between the bilayer and monolayer regions.

We have tested how different couplings between the monolayer and bilayer affect to the device. Figure 6 shows the transfer response of the PdS₂ LH-FET with 9.2-nm long channel, comparing three mixing strategies: 1) the one employed in the manuscript, where the off diagonal elements are assumed to be equal to those of the monolayer region (red circles) 2) a mean of the 1L and 2L coupling values (blue squares), and 3) the bilayer coupling

values (yellow diamonds). We observe that regardless the values assigned to the off-diagonal coupling parameters the transfer characteristic change very little and the $SS < 60\text{mV/decade}$ is conserved.

Band structure

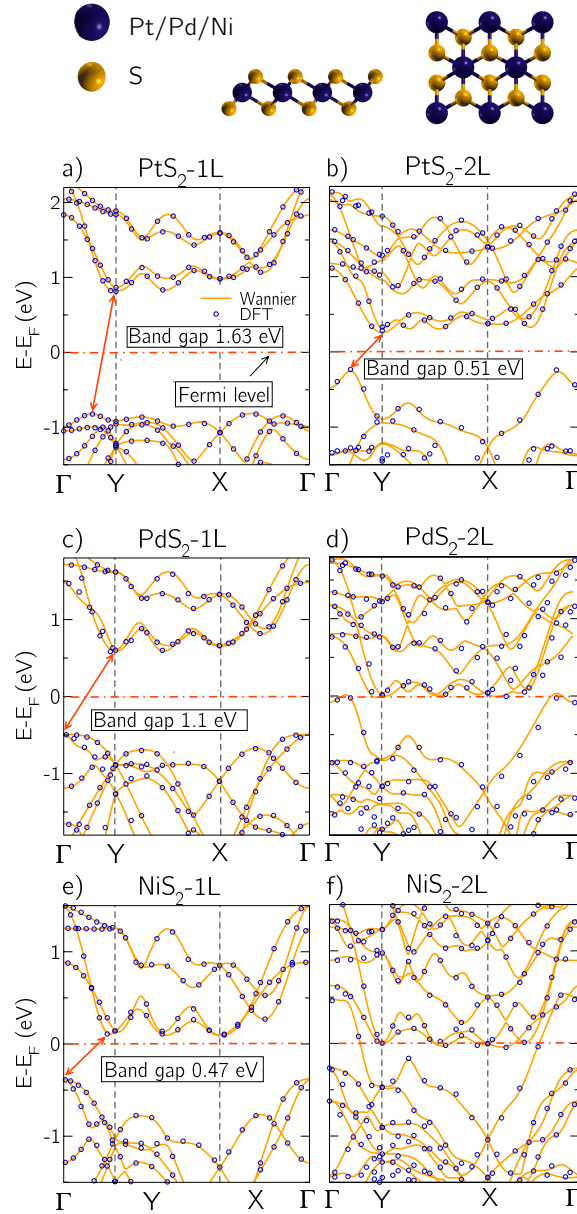


Figure 7: Top and lateral views of the 1T crystal structure of monolayer and bilayer PtS_2 , PdS_2 , and NiS_2 . They are characterized by a 1T structure, with a layer of Pt/Pd/Ni atoms sandwiched between two atomic layers of S. Electronic band-structure on a highly symmetric path along the Brillouin zone as computed with Density Functional Theory calculations (symbols) and with Maximally Localized Wannier Functions (lines).

Schottky Barrier

To deepen in the analysis of the 2L-1L interface and obtain accurate information on the Schottky Barrier (SB) formation and the alignment of the bandstructures of the two regions, we have performed an analysis of a complete 2L-1L heterojunction. First principles calculations using the Quantum Espresso suite³¹ (see Methods) have been performed for the 2L-1L heterojunction. The profile of the vacuum level and the potential profile with respect to the Fermi level, E_F , has been calculated taking into account the formation of dipoles but neglecting the presence of defects. Following the same methodology as in,³⁴ we have extracted values for the SBs of 0.43 eV, 0.26 eV and 0.41 eV for the PdS₂, NiS₂ and PtS₂ lateral heterostructures, respectively. These values have later been considered in the construction of the Hamiltonian for the device simulations.

Current spectrum for the p -type PdS₂ LH-FET

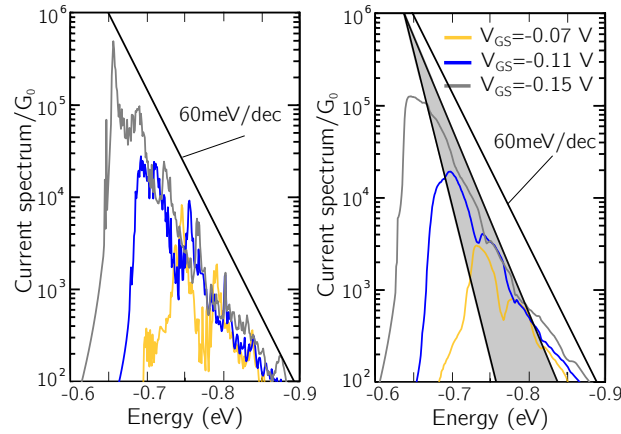


Figure 8: (Left) Current spectrum for the $L_{\text{ch}} = 9.2$ nm PdS₂ LH-FET for the bias points in the p-branch where the sub-maxwellian SS is achieved. (Right) In order to appreciate better the slope of the current spectrum vs. energy we low-pass filtered the current using an average energy window of 5 meV. In shaded gray the range of slopes between 30 mV/decade and 50 mV/decade. The 60 mV/decade Boltzmann limit is also plotted.

Current spectrum for the n -type PdS₂ LH-FET

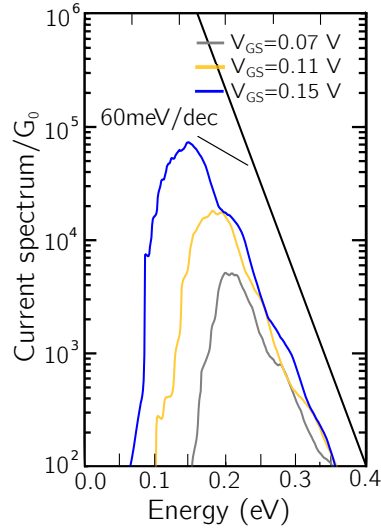


Figure 9: Current spectrum as a function of energy for the $L_{\text{ch}} = 9.2$ nm PdS₂ LH-FET for three different values of $V_{\text{GS}} = 0.07, 0.11, 0.15$ V in the subthreshold region of the n -type branch. The 60 mV/decade Boltzmann limit is also plotted. In order to appreciate better the slope of the current spectrum vs. energy we low-pass filtered the spectrum using an average energy window of 5 meV.

Figures of merit of the PtS₂ LH-FET for low stand-by power applications

Table 1: Figures of merit for several channel lengths of the PtS₂ for low-power applications. Differently from Figure 3 in the main text (evaluated for high-performance applications) the IRDS low-power specifications sets $I_{\text{off}} = 100 \text{ pA}/\mu\text{m}$.

L_{ch} (nm)	<i>n</i> -type				<i>p</i> -type			
	SS (mV/dec)	$I_{\text{on}}/I_{\text{off}}$	τ (ps)	PDP (fJ/ μm)	SS (mV/dec)	$I_{\text{on}}/I_{\text{off}}$	τ (ps)	PDP (fJ/ μm)
5.6	108	$1.1 \cdot 10^6$	1.15	0.04	90	$3.4 \cdot 10^5$	6.1	0.10
7.5	80	$3.6 \cdot 10^6$	0.49	0.09	73	$7.5 \cdot 10^5$	3.4	0.13
9.3	70	$3.9 \cdot 10^6$	0.49	0.10	60	$7.5 \cdot 10^5$	3.8	0.14
11.2	63	$4.5 \cdot 10^6$	0.47	0.11	60	$6.3 \cdot 10^5$	4.8	0.15

Density of states calculation for the 1L and 2L PdS₂

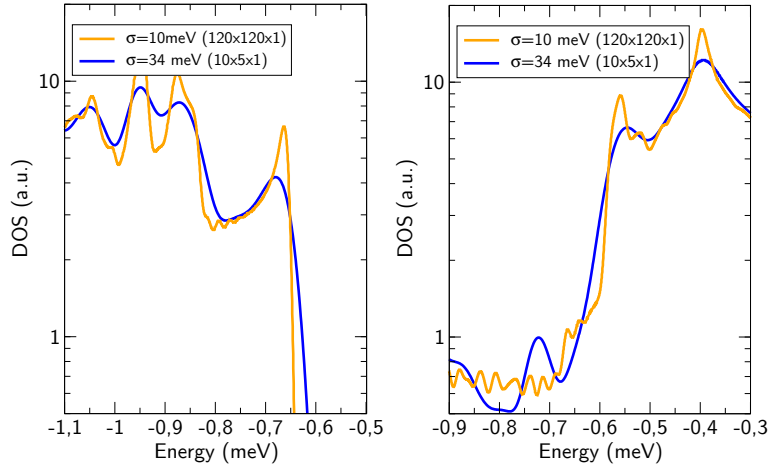


Figure 10: DOS of the monolayer (left) and bilayer (right) PdS₂ in a $10 \times 5 \times 1$ Monkhorst-Pack grid with 0.5 meV of energy resolution and considering a Gaussian smoothing for the energy integration $\sigma = 34$ meV (blue) and in a $120 \times 120 \times 1$ Monkhorst-Pack grid with energy resolution 0.5 meV and after a Gaussian smoothing with $\sigma = 10$ meV (orange).